Deep-learning based monitoring of FOG layer dynamics in wastewater pumping stations

Antonio M. Moreno-Rodenas [a,*], Alex Duinmeijer [b], Francois H.L.R. Clemens [a,c]

[a] Department of Hydraulic Engineering, Deltares, Delft 2600 MH, the Netherlands
[b] Engineering's Consultancy of the Municipality of Rotterdam, Rotterdam, the Netherlands
[c] Norwegian University of Science & Technology, Faculty of Engineering, Department of Civil & Environmental Engineering, Trondheim, Norway

ABSTRACT

Accumulation of fat, oil and grease (FOG) in the sumps of wastewater pumping stations is a common failure cause for these facilities. Floating solids are often not transported by the pump suction inlets and the individual solids can accumulate to stiff and thick FOG layers. The lack of data about the dynamics in FOG layer formation still hampers the design of effective measures towards its mitigation. In this article, we present a low-cost camera-based automated system for the observation of FOG layer dynamics in wastewater pumping stations at high-frequency (minutes) over extended time windows (months). Optical imagery is processed through a deep-learning computer vision routine that allows describing FOG layer dynamics (e.g. accumulation rate and changes in shape) and various hydraulic processes in the pump sump (e.g. the water level, surface flow velocity fields, vorticity, or circulation). Furthermore, the system can perform in-camera image processing, thus allowing the transfer of compressed-processed datasets when deployed in remote locations (Edge AI computing), which could be of great utility for the hydro-ecological monitoring community. In this study, the technology applied is illustrated with a dataset (six months, two-minute frequency) collected at a wastewater pumping station at the municipality of Rotterdam, The Netherlands. This monitoring system represents a source of information for the management of (waste)water pumping stations (e.g. detection of free-surface vortices and scheduling of sump cleaning operations) and facilitates the collection of standardized high-frequency FOG layer dynamics data for a detailed description of FOG build-up and transport processes.

1. Introduction

Uncontrolled accumulation of solids of Fat, Oil and Grease (FOG) in urban wastewater systems has drawn significant public media attention in the past years (for example, the famous 130 tonnes 'Fatberg' found in Whitechapel London and others, Adams, 2018). Despite an increase in public awareness, urban disposal of cooking oils and fat through wastewater transport systems still produces significant build-up of FOG solids. An international review by Wallace et al. (2016) found that this problem is ubiquitous and that its severity depends on the design and age of the wastewater system, disposal habits of citizens and mitigating measures (e.g. grease trapping). The presence of FOG solids in wastewater transport systems induces reduction of hydraulic capacity (Ashley et al., 2000), urban flooding, sewage spills (imposing health risks, Ten Veldhuis et al., 2010) and damage to pumping stations (Duinmeijer, 2020).

For urban drainage systems, a reliable operation of wastewater pumping stations (WWPS) is critical to effectively meet their functional requirements (Korving et al., 2006). The presence of multiple phases and related transport phenomena (transport of solids, entrainment of gas/air) is known to increase WWPS failure rates. Meanwhile gas accumulation processes are well understood and managed (Pothof, 2011), floating FOG accumulation in pump sumps are less known and receive little attention in guidelines for pump sump design (e.g. (American National Hydraulic Standards Institute 2012)).

The sump geometry and configuration of most WWPS do not guarantee the transport of floating solids to wastewater treatment facilities. Furthermore, oil and fat deposits experience chemical and physical transformations (e.g. saponification, Keener et al., 2008 and He et al., 2013) which hardens the material. The mixture of hardened FOG with additional materials such as textiles or plastics form a structurally stable stiff layer, often covering the entire sump surface (Duinmeijer and
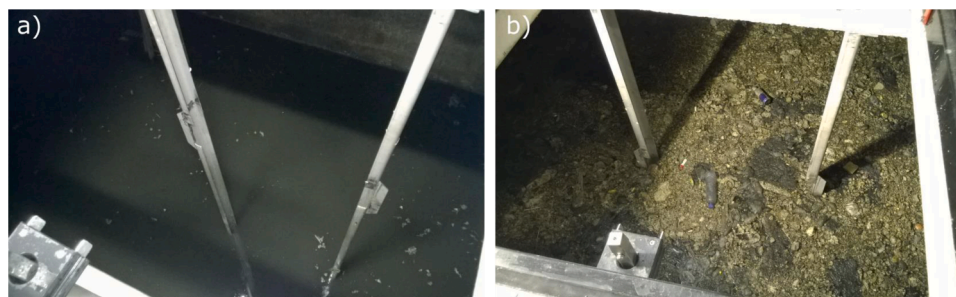
Fig. 1. Accumulation of loose floating FOG solids (a) to a closed stiff FOG layer that covers the entire sump surface (b).
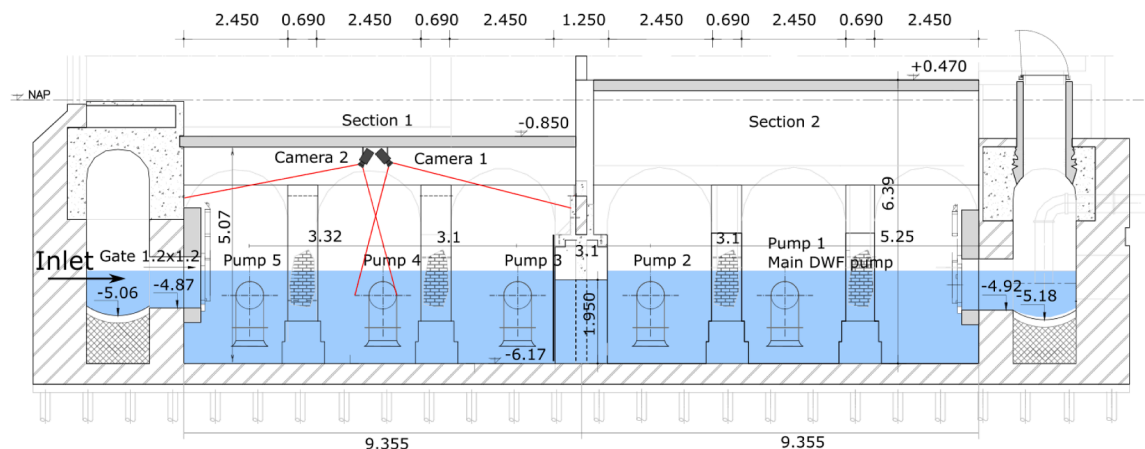

Fig. 2. Side-view of the sump of the Pretorialaan WWPS with approximate camera locations and camera view field. The dimensions are in meters.

Clemens, 2016), see Figure 1 and more examples in Appendix A.

Manual removal of FOG layers results in high operational costs and is a health hazard for the personnel involved. For all WWPS in the municipality of Rotterdam, the annual FOG removal cost is approximately € 400.000 (requiring ~8.000 work-hours per year, 2020). Extrapolating this figure, we estimate a cost on the order of €10 M/year in The Netherlands. Similar estimates are reported for the UK with 15 to 50 million pounds (€18-60 M in 2016) per year (Wallace et al., 2016). Furthermore, FOG disposals are also regarded as a potential source of energy (i.e. biofuel, see Jolis et al, 2010, Miot et al, 2013, Pastore et al, 2015) and hence holds potential economic value which is still not widely exploited. For any FOG management strategy (mitigation, collection/-reuse/recycling) to be feasible and successfully implemented, data on FOG layer dynamics (i.e. accumulation rate and transport mechanisms) are required.

Despite the economic and environmental relevance of this problem, knowledge of FOG layer dynamics at WWPS facilities is currently limited. This is mainly due to a lack of understanding of the processes involved (transport, (bio)chemical transformations and evolution of physical properties), the highly heterogeneous catchment characteristics and the fact that obtaining measuring data in sewers, given the physical/chemical conditions and the poor accessibility of these systems, is challenging. Nevertheless, some observational data have been reported in the literature. For instance, Nieuwenhuis et al., (2018) found correlations of FOG solids accumulation with socio-economic parameters of the service area. Williams et al., (2012) showed links of FOG solid formation and local water composition. However, the discrete[1] nature of this data hampers a quantitative assessment of the transport and

accumulation processes involved. To the authors' knowledge high-frequency data of FOG layer dynamics is missing.

Camera-based monitoring of water processes is rapidly popularizing due to access to relatively inexpensive hardware (Pagnutti et al., 2017) and community driven open access software initiatives (e.g. OpenPIV or Opencv). In urban drainage, we can find examples such as the observation of in-sewer processes (Shahsavari et al., 2017 and Regueir-o-Picallo et al., 2020) or the estimation of flow around drainage structures (Leitão et al., 2018, Duinmeijer et al., 2019, Martins et al., 2018 and Naves et al., 2021). Furthermore, computer-vision deep--learning (DL) routines allow extracting complex information from videos and images. DL allows exploiting spatial and contextual cues from imagery to extract information relevant for tasks such as object detection or classification. When sufficiently trained, these systems are robust to environmental changes (e.g. lighting, visual conditions) and can be deployed in the field. For instance, for the determination of flooding area estimates (Jiang et al., 2019 or Moy de Vitry et al., 2019) or lab-scale model surface classification (den Bieman et al., 2020). The synergies of computer-vision and DL applications will likely increase the number of variables that we are capable to measure in hydro-ecological environments (Valero et al., 2021) and for which the urban drainage community should adapt (Blumensaat et al., 2019).

This article presents the design and deployment of an embedded-camera system for long-term and high-frequency automated monitoring of FOG layer dynamics in the sump of WWPS that is non-invasive, scalable and robust. A deep-learning routine was built and used to process large quantities of WWPS top-view images for the detection of FOG layers. We showcase the application of this system with a dataset of 6-months (2 minutes frequency) collected at a WWPS in the municipality of Rotterdam. Also, we discuss the possibility of extracting additional variables of interest for the management and control of WWPS (e. g. water level, surface flow velocity fields and vorticity estimations).

The outline of the present article is as follows: The hard and software
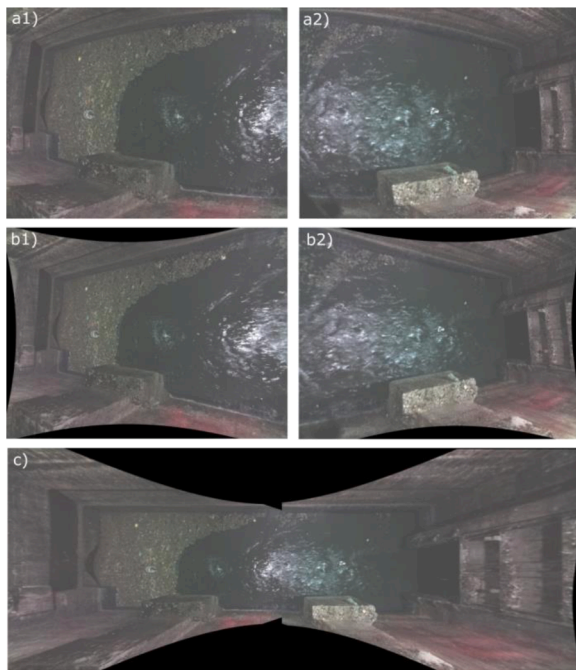
---

[1] The term 'discrete' here refers to 'observations made only once or with irregular time intervals' that do not allow for quantification of the underlaying dynamic processes.

Fig. 3. Image pre-processing example. (a) Raw images from camera 1 and 2, (b) undistorted image, (c) perspective correction and mosaic.

designs are described in section 2 Materials and methods. Section 3 reports and discusses the results obtained in two pilot wastewater pump sumps. Finally, section 4 addresses the overall conclusions along with suggestions for future research and applications.

2. Materials and methods

2.1. Case studies

2.1.1. WWPS Pretorialaan

This pumping station discharges wastewater from a combined sewer system in the south of Rotterdam (the Netherlands) to a wastewater treatment facility. The connected catchment has a size of approximately 650 ha and 120,000 inhabitants. The sump of the WWPS has a rectangular geometry of 18×3 m (surface area), see a side-view in Figure 2. Waste- and stormwater enters the sump by a 1.2×1.2 m inlet with soffit level at -4.87 m NAP (Amsterdam Ordnance Datum). The station has five pumps for the discharge of wastewater (pump 1) and stormwater (pumps 2 to 5). Pump 1 has a fixed capacity of $\sim$1200 m^3/h. Pump 2 to 5 has a variable capacity of 1500 to 2000 m^3/h. In the middle of the sump there is a small restriction in the cross-sectional flow area (1.9×2.1 m). This restriction is used as dividing line for splitting up the sump in two sections (section 1 and section 2, see Figure 2). Two cameras were installed in section 1 one day after the operators cleaned the sump (28-07-2020).

2.1.2. WWPS Nieuw Terbregge

This WWPS is also located in Rotterdam and discharges wastewater from a separated sewer system. The connected catchment has a size of $\sim$ 61 ha and $\sim$ 2000 inhabitants. The sump has a rectangular geometry of 1.6×2.5 m. The wastewater enters the sump by an Ø600 mm inlet and discharges by two submersible pumps with a fixed capacity of about 35 m^3/h each. A set of flanges were installed in the inflow channel to promote circulation in the pump (Duinmeijer 2020) and investigate the formation of surface vortices. A top-view camera was installed at this station. Data from this station is used in this study to showcase the potential to derive surface velocity fields and vorticity estimations in pump sumps.

2.2. Monitoring system

The camera system was composed by a programable micro-computer (Raspberry pi 4+ 4GB RAM, Raspbian Linux OS), an 8-megapixel camera (Sony IMX219) mounting a 98°FOV fisheye lens (ENTANIYA RP-L98). A custom-made 3D printed case was constructed in ABS plastic with a protective paint coating and an acrylate lens protector. The enclosure had a stainless steel backplate to ensure good thermal dissipation of the hardware. Figure B1 (Appendix B) contains a graphical depiction of the camera case and power-supply box. Three LED floodlight lamps (KONIG LED, 750 lumens, 10W) were used to illuminate the basin and were mounted below three access gates. Waterproof connectors and the tailored design of the enclosure aimed at reducing corrosion and gas/condensation damage to the camera system.

Two of these cameras were deployed (FATracker 1 and 2) at section 1 of the Pretorialaan station ($\sim$9 $\times$ 3 m) as shown in Figure 2. The cameras were installed below one of the maintenance access gates to the basin at approximately -1.2 m NAP. Water level was maintained at an average of -4.2 m NAP and a maximum level of -1.94 m NAP was recorded during the measurement campaign. The cameras had a 5V power supply and 4G connection for remote operation and data transfer (provided by a router TP-Link TL-MR6400). Individual images were acquired using a shutter-speed of 100 ms, ISO-800, 1024×768 px resolution at 2 minutes interval. Two consecutive images (at a user defined Δt) could also be collected for estimating displacement fields. Operational and maintenance access was granted through a 4G VPN network, email alerts were scheduled for camera thermal levels (none were triggered during the observation period).

A third camera was installed at *Nieuw Terbregge* WWPS to investigate the formation of surface vortices in 2018 (see Duinmeijer 2020). This consisted of a commercially available IP-camera (Axis M1125-E), recording at 30 images per second with a resolution of 480×640 px in a top-view configuration. Images were transferred through 4G network to a centralized server at the municipality of Rotterdam. Imagery of this camera is used in this study to showcase the potential use of top-view imagery to derive surface velocity characteristics (and vorticity) in a WWPS.

2.3. Image pre-processing

A pre-processing routine was applied to images collected in order to: i) Correct for lens and sensor optical deformation (intrinsic calibration), ii) rectify the water plane perspective and iii) mosaic images to create a seamless basin image. The python library OpenCV (Bradski, 2000) was used for the camera calibration and perspective rectification of the images. 15 images of a 17×21 chessboard pattern with 25 mm squares were taken at different orientations and positions from each camera. A fish-eye camera distortion model (OpenCV manual, 2014) was fitted to the detected checkerboard squares and used to correct for lens and sensor distortions (Figure 3, b), thus preserving linear features in the image.

The cameras installed in Pretorialaan were top-down oriented at $\sim$45 degrees with the horizontal plane, this induced a perspective distortion of the water plane which was corrected using known corresponding image-pump sump positions. A perspective-warping model was applied to create 4-point perspective transform to a water plane top-view position and to mosaic both camera views (Figure 3, c).

2.4. Semantic-segmentation of FOG layer images

A convolutional neural network (CNN) routine was developed to discriminate between and locate three types of surfaces (FOG, water and superstructure) in pump sump images. The network was built using Tensorflow (Abadi et al. 2016) and takes the form of a semantic-segmentation (Sem-Seg) architecture (Garcia-Garcia et al., 2017 and Ye and Sung, 2019). This algorithm processes RGB-image data
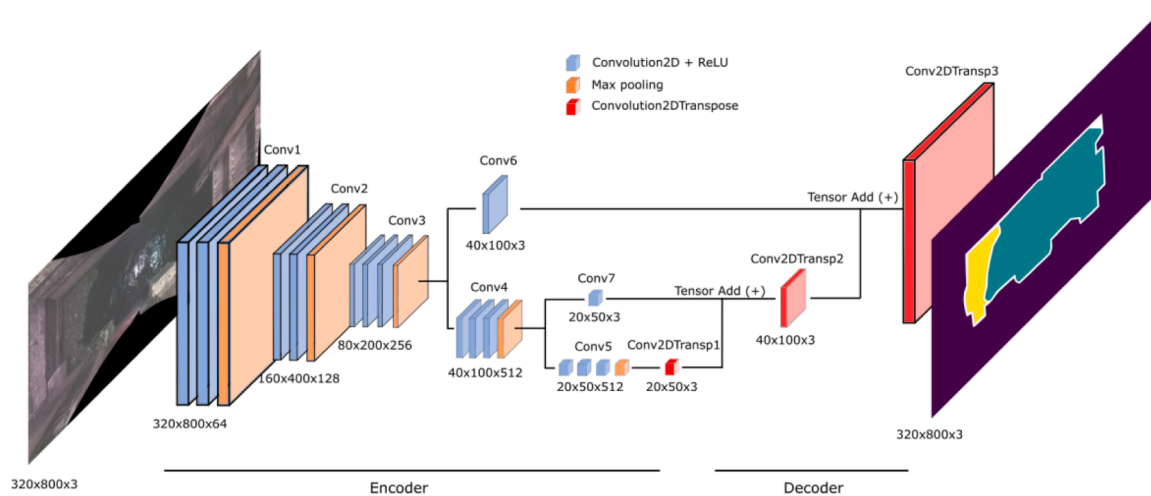
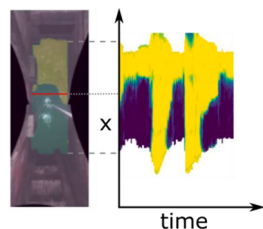**Fig. 4.** Semantic-Segmentation CNN architecture scheme.

Fig. 5. Scheme for the time-dependent length-wise FOG layer position dynamics.

to retrieve dense labelled regions (spatial localization and classification) from a pre-selected list of objects or surfaces of interest (i.e. WWPS superstructure, FOG and water extent).

The network architecture was configured as a VGG16 (Simonyan and Zisserman, 2014) encoder, and a fully convolutional network (FCN) decoder (Figure 4). We used transfer learning to reduce the number of FOG labelled images required during training. To that effect, we initialized the encoder (VGG16 network) parameters with weights pre-trained on the *ImageNet* dataset (Deng et al., 2009), a multi-million labelled image public repository. This allowed acquiring a relatively general set of encoder filters capable of performing object classification before the application to FOG layer detection. A sparse categorical cross-entropy loss function was used to update the network parameters.

Representative images across different water level and FOG layer extent states were manually selected to create a training database. A total of 89 mosaicked images (see Figure 3), c) were manually labelled (by the same individual), hence supplying masks of the extent of FOG layer, water and pump superstructure (e.g. walls, cables/pipes, gates etc.). A data augmentation routine was applied to increase the training size by mirroring all labelled images. Thus, a total of 178 labelled images were used during training and validation of the network with a split of 70%-30% (124 training, 54 validation). During training, both encoder and decoder parameters were updated. Training was performed during 250 epochs using a batch of size of 15 examples. An NVIDIA Tesla Turing 4 GPU (16GB, 8.1 TFLOPS) was used during the learning and testing phase.

During processing, images from both cameras were undistorted and mosaicked to create the optically-corrected basin top view. Then, input images were resized to the input size of the Sem-Seg network (320 × 800px) and processed. Class-encoded output masks were upscaled back to the original mosaic size (640 × 1660px) and were fed to the post-processing algorithm, which computed geometrical properties of the FOG layer over time.

The image segmentation routine was carried out offline using a NVIDIA Quadro T2000 GPU (4GB) with a processing time of 1.2 seconds per image. Also, in-sensor inference could be achieved at the camera (using a Raspberry Pi 4 Model B, ARM CPU Quad core Cortex-A72) with a processing time of 9.8 seconds per image. The camera could hence work in two modes, in-situ processing and transferring processed masks (reduced data transfer) or transfer raw RGB high-resolution images for offline postprocessing.

2.5. Post-processing

2.5.1. FOG-Water surface ratio

Masks provided by the Sem-Seg CNN output classify regions of water-FOG-superstructure. A computer-vision algorithm was created to retrieve the extension and location of the layers over time. This consisted in a morphological opening and closing operation on the raw masks (border smoothing and noise filtering), extracting contours from the labelled mask and computing surface areas. Since images were perspective-rectified for a top-view of the basin, we assumed that the ratio between water surface and surface covered with FOG was approximately depth-invariant.

Instantaneous FOG-water ratio was computed using the Sem-Seg derived FOG top-view pixel area (A_{FOG}) and the water pixel area (A_{Water}) as:

$$FOG \Big/ water\ ratio = \frac{A_{FOG}}{A_{FOG} + A_{Water}} \qquad (1)$$

Additionally, in order to visualize FOG layer dynamics, we computed the along-length FOG/water pixel density average (from the inlet to the pump sump separation wall) as depicted in Figure 5, thus displaying a length-time 2D FOG pixel density.

2.5.2. Cameras for water level estimation (optical gauge)

Exploiting image-data to extract water level information is a promising strategy to leverage the growing number of CCTV networks in cities worldwide. For instance, Jiang et al., (2019), proposed extracting street flooding water levels by comparing landscape features of known shape. (Moy de Vitry et al., 2019), on the other hand, proposed a simple water-area proxy as a correlated variable to water level in street video data. Here, we applied a similar approach to de Vitry et al., 2019 to derive sump pump water level data as a by-product of the FOG monitoring system. We used the observed wet area ($A_{wet_{cam}} = A_{FOG} + A_{Water}$, in pixels) to define a distance-to-camera proxy. However, since our imagery was strictly a top-down view of a rectangular basin (as opposed to street-camera applications), we used the square-root of the

Table 1
Sensor characteristics.

Variable	Freq	Unit	Resolution	Characteristics
Water level at the pumping station (Pretorialaan)	1 min	m	±0.075% water depth	Pressure gauge Endress+Hauser type FMB70
Pump flow (Pretorialaan)	1 min	$m^3 \bullet s^{-1}$	±0.5% flow rate	Electromagnetic flow meter
Rainfall intensity	1 h	$mm \bullet h^{-1}$	±0.1 mm/h	KNMI Station ID-344 Rotterdam
FATracker 1 and 2 (Pretorialaan)	2 min	px	1024 × 768 px ~10.6 mm/px (mean)	Camera (Sony IMX219) Processing unit (ARM Cortex-A72)
IP-Camera (Niew Terbregge)	30 fps	px	480 × 640 px ~ 6.2 mm/px (mean)	Camera (AXIS M1125-E)

instantaneous wet area to transform to a length-proxy dimensions. Synchronized water level measurements (d_{obs}) during a period of 8 days (25-09-2020 – 02-10-2020) and two-minutes frequency were used to calibrate a regression model from the proxy optical-gauge ($A_{wet\_cam}^{0.5}$) to an estimated basin water level ($d_w^{'}$). A gaussian process regression model (GP) was adjusted in the following form:

$$
\begin{aligned}
\boldsymbol{d}_{w}^{'} &= f\left(A_{wet_{cam}}^{0.5}\right) + \varepsilon \\
f(\cdot) &\sim GP\left(0,\ k(\cdot, \cdot)\right) \\
\varepsilon &\sim N\left(0,\ \sigma^2\right)
\end{aligned}
\tag{2}
$$

with $k(\cdot, \cdot)$ a squared exponential covariance matrix ($k(x, x^{'}) = e^{k_p \|x, x^{'}\|^2}$, k_p a scale parameter) and ε a random variable of gaussian i.i.d noise. The calibrated regression model was used to obtain an optically derived water level estimated in the full time-series and was validated using a time-series of 30 days (2 min frequency, 20-08-2020 – 20-09-2020).

2.5.3. Particle tracking velocimetry and vorticity estimations

Velocity data of the surface flow in the sump can also be derived as a by-product of the camera installation. This requires the presence of optical tracers (e.g. debris or FOG solids) to be captured by subsequent images (Jeanbourquin et al., 2011), or by seeding the domain with a visual tracer (e.g. fluorescent particles, Naves et al., 2020). These tracers can be used to find spatiotemporal correlation patterns and retrieve velocity fields by Particle Image Velocimetry (PIV, Adrian and Westerweel, 2011), or Particle Tracking Velocimetry (PTV, Agüí and Jiménez, 1987).

To illustrate this, we use imagery from the *Nieuw Terbregge* station. The geometry of this station was modified with a deflector flange installed at the inlet to enhance flow circulation and promote the generation of free-surface vortices (Duinmeijer 2020), an undesirable

process for the operation of pumping systems. We acquired consecutive images with a frequency of 1.51 Hz (each 20 frames). These were undistorted and perspective-corrected at the water plane (as described in Section 2.3). A sequence of 244 images was used to derive particle-tracking velocimetry (PTV) for the quantification of the surface velocity field ($\vec{u}$) and flow vorticity ($\vec{\omega} = \nabla \times \vec{u}$) from the floating particles embedded in the flow. The signal-to-noise ratio in the images was improved using an ensemble background subtraction and a manually defined area of interest. An initial velocity estimation was obtained by a sum-of-correlation (SOC) approach with 2 passes at 16 × 16 px with 50% overlap. Particle tracks and velocities were derived using the 2D-PTV algorithm from DaVis PIV software (LaVision, version 8.0) using the SOC field as initial displacement. Vorticity was computed directly from the (SOC) velocity field.

2.6. Additional datasets

A set of additional measured variables were used to describe the interaction of the FOG layer with different processes of the WWPS. Table 1 presents the main characteristics of all sensors used in this study.

3. Results and discussion

3.1. Semantic segmentation of FOG surfaces

The weights of the Sem-Seg CNN structure were updated during 250 epochs when training. This resulted in a final loss of 0.051 and 0.054 for training and validation respectively, corresponding to 97.9% and 97.8% accuracy. The progression of loss and accuracy during training is shown in Figure 6. The results of training and validation of the Sem-Seg CNN routine were deemed appropiate for the application.

A collection of 30 manually-selected images at representative states of water-level and FOG cover (outside the training and validation datasets) were used to visually assess the behaviour of the Sem-Seg algorithm. Figure 7 shows the output at six random samples of the 30 cases. The color-coded classification mask is shown in the middle column and a merged raw input and classified mask is shown in the right column.

We processed ~106,000 images captured at the WWPS Pretorialaan generating masks for surface class (i.e. superstructure, FOG and Water). Figure 8 shows an example of the detection of water and FOG cover at a time-snapsot.

3.2. Analysis of FOG layer dynamics

Figure 9 shows the time-series processed at the WWPS Pretorialaan with measured rainfall intensity, measured sump water level and sewer inflow. The image-derived dynamics of the FOG/Water layer capture the
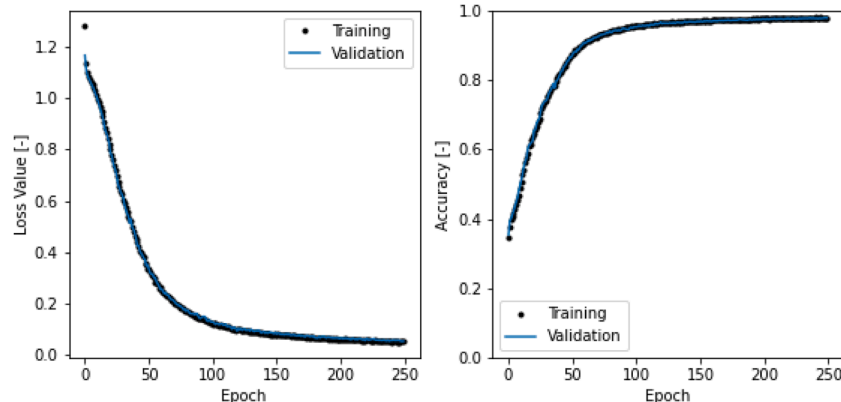

Fig. 6. Training and validation loss value (left) and accuracy (right) after 250 epochs of training.
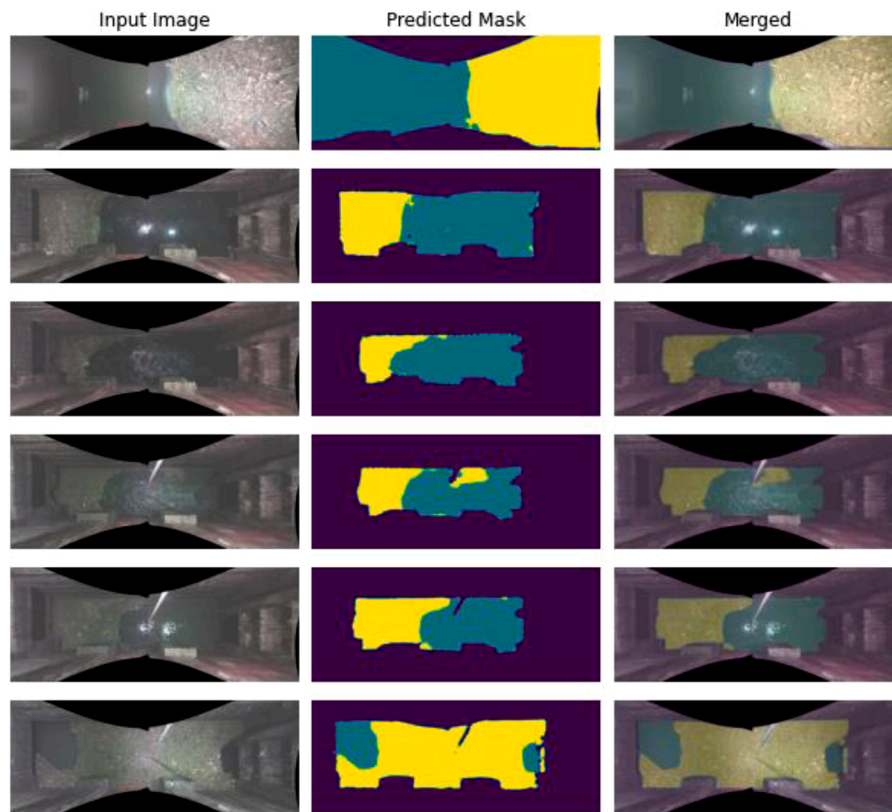
Fig. 7. Input image and predicted multilabel mask (green - water, yellow - FOG and purple – superstructure) at six test images independent from the training dataset.
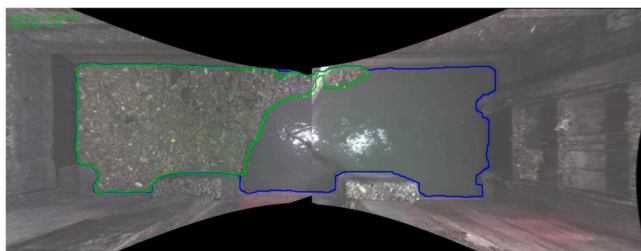

Fig. 8. Example for a mosaicked and rectified pump sump view with overlay of the CNN-classified water and FOG cover zone at the WWPS Pretorialaan. Image corresponding to 25-10-2020 00:27 with a 47% FOG ratio cover.

progressive FOG build-up from the initially clean sump. The WWPS sump went from a FOG/Water surface ratio of 2% on the 28-07-2020 until a 77% on the 31-01-2021 (187 days) computed as a 10-day rolling mean. A video animation of the full dataset can be found in Appendix D.

Data derived from the optical location of FOG-water surfaces in the sump, can be used to assess the accumulation and transport of FOG solids over time. Additionally, this data provides valuable information to understand interactions between the sump geometry, and the WWPS operational rules. Figure 10 presents a detailed analysis of a 13-day period (03-11-2020 – 16-11-2020), depicting FOG/water ratio (2nd row) and the length-wise FOG layer location dynamics (3rd row). We could observe that the FOG layer dynamics are strongly influenced by the water level, pump discharge and pump operation pattern.

During dry-weather flow (DWF) the FOG layer presented stable fluctuation (minute-day timescale) due to the intermittent variation of kinetic energy generated by the inlet flow and the DWF pump switch-on/off levels (pump 1, see Figure 2). The inlet flow mobilizes the FOG layer mass shifting it towards pump 1 (sump section 2). High inflow

during storm events (wet weather flow, WWF) leads to an increase of water level in the pump sump and the activation of storm-water pumps (pump 2 to 5). The FOG layer extent showed a strong sensitivity to water level. This could be explained by the hydrodynamics in the sump; at high water level, the flow of FOG towards the sump section 2 is blocked by the restriction in the middle of the sump (Figure 2). Simultaneously, the submerged inlet inflow and the activation of WWF pumps creates a surface recirculation pattern in the sump extending the FOG layer towards the inlet. A similar behaviour in the dynamics of the FOG layer is observed in the 13th of October, when pump 1 was temporally disconnected and a higher DWF pump switch-on water level was maintained during several days. This increased water level resulted in a restriction of FOG flow towards the pump section 2 and the reduction of the sewer inflow velocity, thus producing a larger FOG layer length-wise amplitude than with the previous DWF settings (see Figure 10).

It should also be noted, that the field of view (FOV) of the camera mosaic did not cover the entire sump surface at extreme high-water levels. For a sump water level above $-3.5\ m$ the water surface-view exits the FOV of camera 1. The entire mosaic FOV was covered by the water surface at an approximated depth of $-2.8\ m$ (see Figure 7, first row). The degree of FOV cover can be seen at Figure 10 (middle graph) which shows the length-wise location of the wet (FOG and water) cover with respect to the camera view. This may induce a bias at high-water level and should be taken into consideration during the design (e.g. use of wide-angle lenses) and analysis of the FOG measurement campaign.

During the observation period the system suffered several incidents that required maintenance. An automated sampler (to monitor evolution of SARS-CoV-2) was installed in view of camera 2 from 08:46 10-09-2020 onwards. The Sem-Seg algorithm filtered this view obstruction (see examples 4, 5 and 6 in Figure 7). Also, camera 2 suffered intermittent loss of connection during three periods (seen in the FOG data gaps in Figure 9). This has now been remediated by the installation of a connection monitor-device. It should also be noted that the dataset
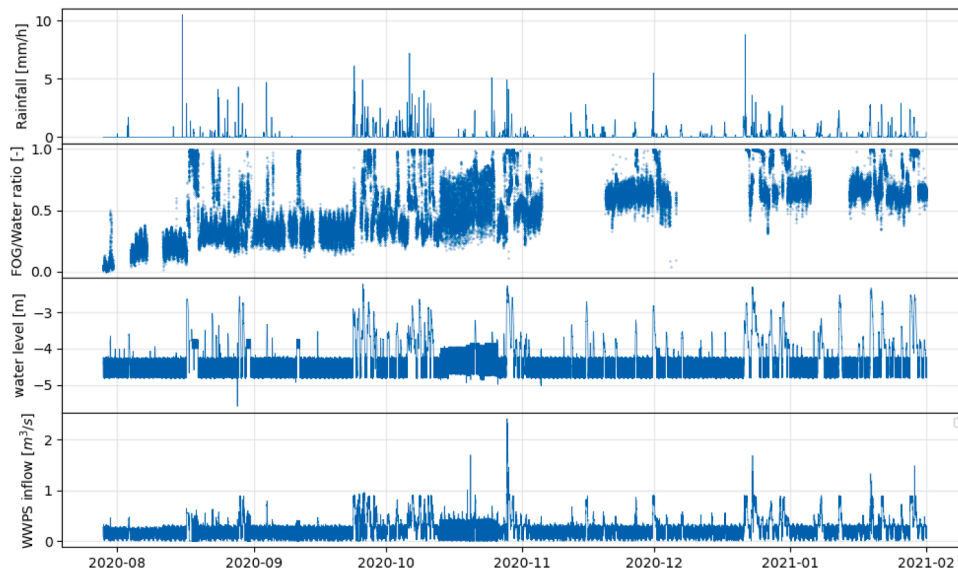
Fig. 9. WWPS Pretorialaan processed timeseries. Rainfall, image-derived FOG/Water ratio, measured water level and estimated WWPS inflow (derived from pump discharge and water level changes).
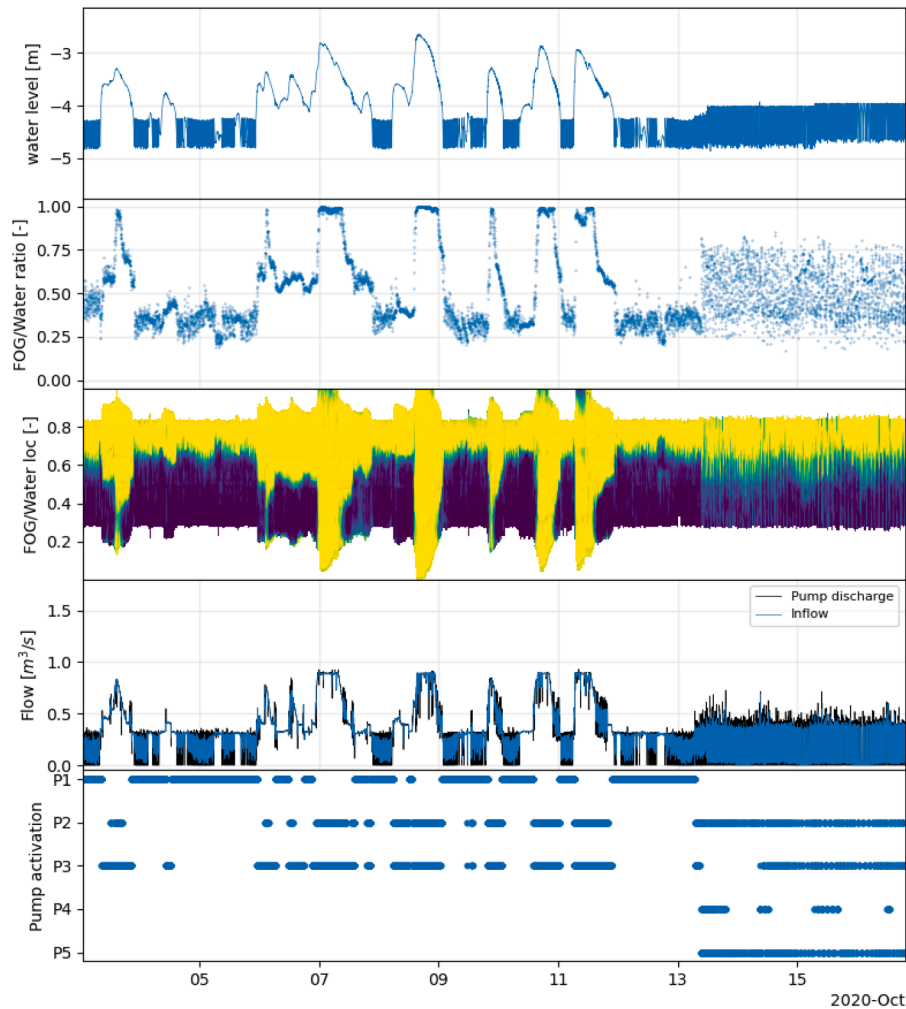

Fig. 10. Detailed FOG layer dynamics. In order from top to bottom: i) Water level (m NAP referenced), ii) FOG/water ratio, iii) Length-wise FOG spatial location (cross-section percentage of FOG (yellow) to water (blue) from the inlet section to the rear wall), iv) pump discharge and estimated WWPS inflow (from sewer) and v) pump operation pattern.
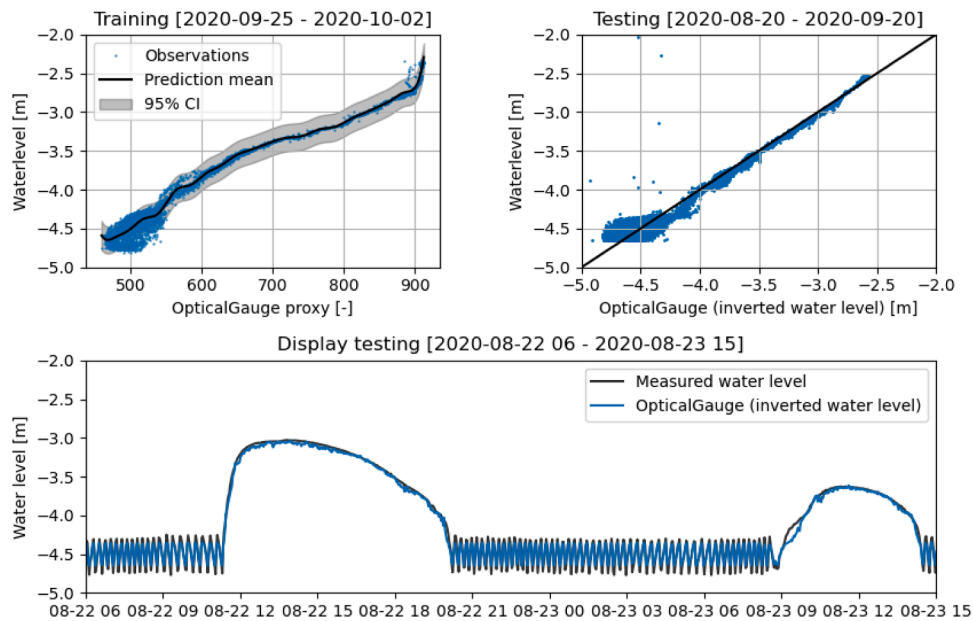
Fig. 11. Cameras as an optical water level gauge. A Gaussian process regression model was fitted for water level measurements and an optically derived depth proxy (top-left). At the top-right, comparison of optically derived water level vs. measured at an independent test dataset (30 days). The graph at the bottom presents a 1 day time-series (2-min resolution) of water level measurements and optically-derived water level.
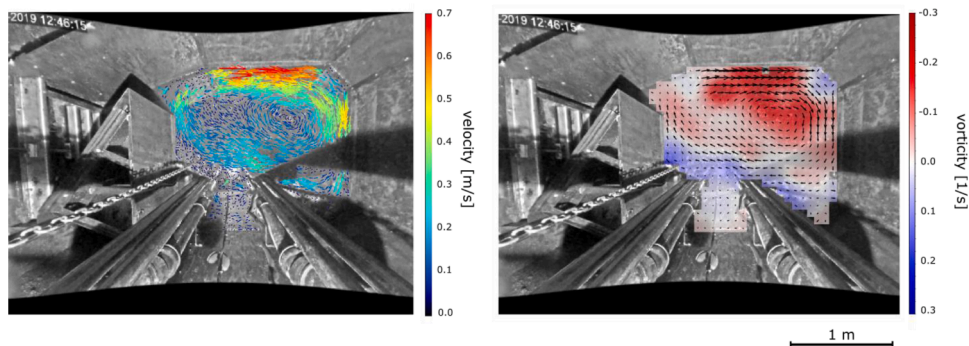

Fig. 12. Surface flow particle-tracking velocimetry (left) and vorticity (right, shown together with arrows displaying velocity direction and magnitude) estimations in the sump of the WWPS Nieuw Terbregge.
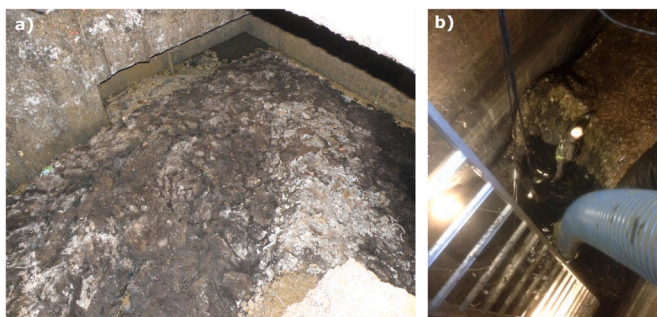

Fig. A1. Detail of a stiff FOG layer at the Pretorialaan WWPS (a), and (b) cleaning of a 1.8-meter thick stiff FOG layer in the W.M. Schurmannstraat WWPS (source: municipality of Rotterdam).

Fig. A2. Cleaning of the FOG layer at the Hoekersingel WWPS (source: municipality of Rotterdam).

presented was gathered from 28-07-2020 until 31-01-2021. Most of this period was under the influence of restrictions (of varying severity) to mitigate the COVID-19 pandemic in the Netherlands (see Figure C1, Appendix C). Consequently, this data might capture changes in behavioural patterns in the population (due to restrictions) and might not be

fully representative of a pre- or post-pandemic situation.

3.3. Cameras as an optical-gauge for water level estimations

Water levels were derived from a regression model (see eq. (1)) that transformed the camera view wet-area extent to a water level estimate. Figure 11 shows the results of training and testing the optical-gauge model. In the top-left, the gaussian process model mean and 95% CI is shown. It is to be noted, that intermediate/high water level was well
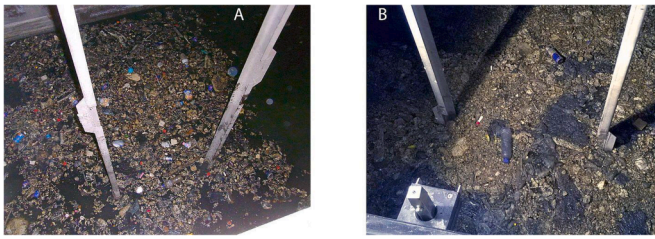
Fig. A3. Accumulation of loose floating FOG solids (A) to a closed stiff FOG layer that covers the entire sump surface (B), (Duinmeijer, 2020).
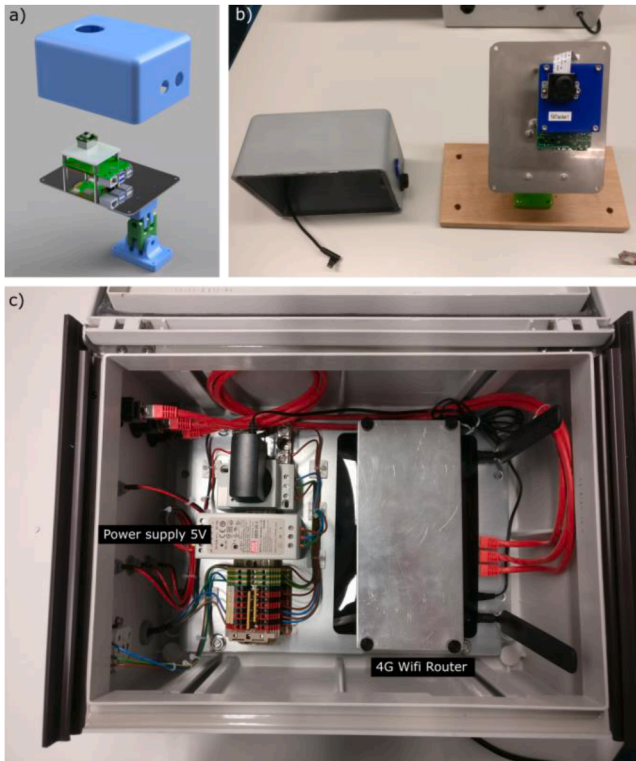

Fig. B1. Hardware scheme. a) 3D design of the camera case, mount and pivoting camera stand. b) Raspberry pi and camera physical layout. c) Setup box with power supply, 4G connection and lighting control.
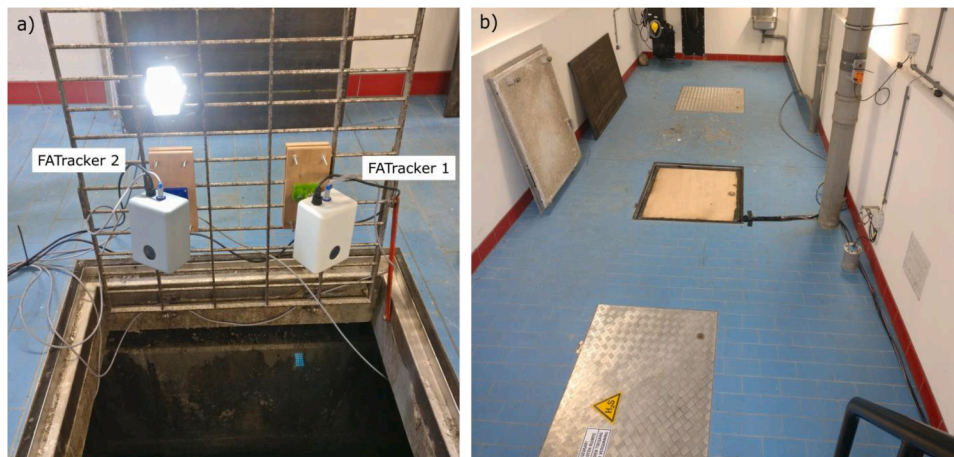
captured. We observed an increase in variance at low water levels, explained by the top-view perspective that is expected to reduce surface differences with increasing camera-to-object distance. On the other hand, extreme water level ($d_{obs} > -2.8\ m\ NAP$), which fully cover the camera view could not be derived (denoted by the change in slope at the end the regression plot, Figure 11, top-left). Using the period of 20-08-2020 to 20-09-2020 (31 days, 2 minutes frequency) as a test dataset, resulted in a root-mean-square error of 0.11 m and a Nash-Sutcliffe efficiency of 0.901. This shows, that once calibrated, the optical-gauge can be used as a reliable source of water level information for wet to dry weather flow transitions or as a redundant alarm system for pump malfunction events. Higher accuracy can likely be achieved with a dedicated design, for instance deploying a calibrated high-contrast object (e.g. white board in a wall) or optimizing the camera position for water level observations.

3.4. Surface flow velocimetry and vortex detection in pump sumps

Figure 12 shows the estimation of a surface flow velocity field by means of PTV (left) and the estimation of the flow vorticity (right) in the sump of the WWPS *Nieuw Terbregge*. These measurements may be affected by the slip between the tracer and the water flow and thus underestimate the real flow velocity. The severity of this bias will depend on the particle-flow characteristics (i.e. mass, superficial density and lumping/aggregation phenomena). The extent and correction of these processes remains to be further investigated. We observed that tracers appear to be between 0.01 to 0.2 m, and often mix buoyant objects of different nature (e.g. plastic litter) with ellipsoidal FOG lumps. An example of the raw imagery used for the PTV processing can be found in Appendix E. Also, Appendix A, Figure A3 (A) shows a typical high surface density tracer distribution at a different WWPS.

Nevertheless, these estimated flow velocity and vorticity fields represent a relevant source of information (even qualitatively) about surface particle motion and may be used for the detection of free-surface vortices in the pump sump (highly relevant for the pump operation).

4. Conclusion

This study describes the use of a programable camera system that can be deployed in (wastewater) pumping stations and can acquire and automatically process high-frequency data of FOG layer dynamics. The relatively inexpensive hardware involved makes the technology widely accessible. Estimation of the FOG layer cover through the deep-learning routine resulted in a performance comparable with human classification (0.978 accuracy during validation). This AI solution shows a good
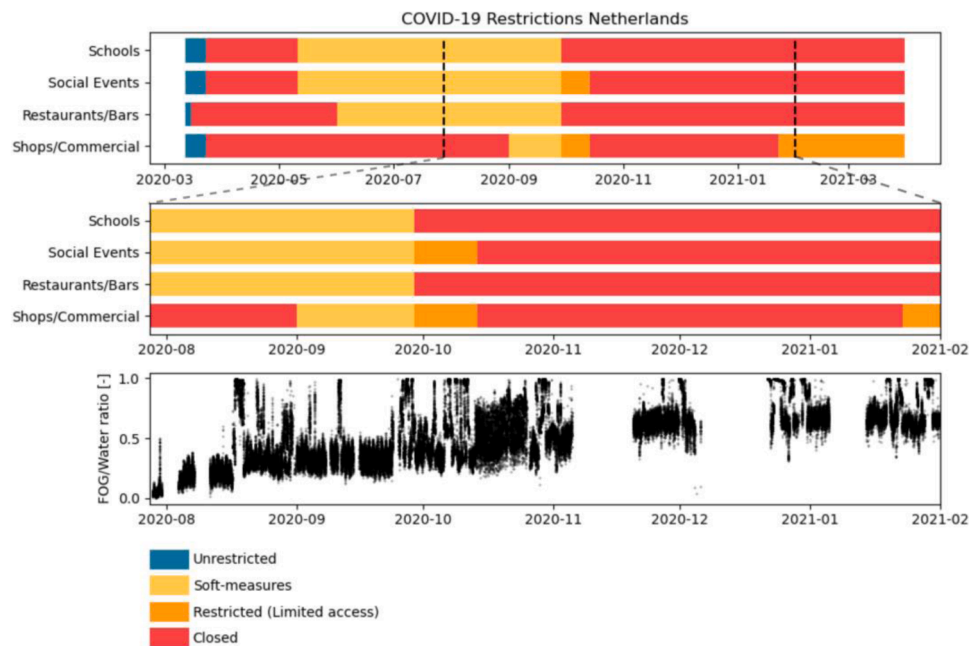

Fig. B2. Installation detail for a) camera mounts (camera 1, right and camera 2, left) and b) final enclosing of cameras with a water/gas-tight gate at the Pretorialaan station.

Fig. C1. Covid-19 pandemic restrictions for Schools, social events, restaurants and public commercial businesses during the monitoring period of this study.
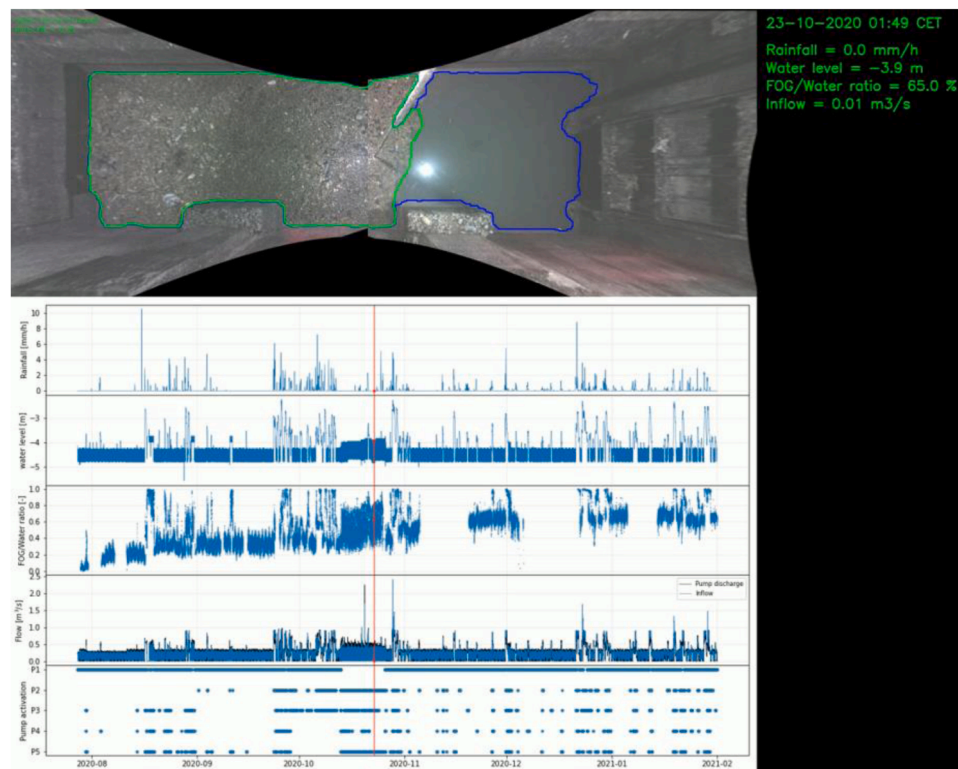

Fig. E1. Example of raw imagery from the Nieuw Terbregge WWPS used for deriving particle tracking velocimetry fields. a) and b) represent two RGB frames taken at 0.66 s difference, and c) shows the processed particle velocity field.

scalability since it can efficiently process large amounts of data (high-frequency, long term monitoring) with a reduced initial investment (manual labels). The Sem-Seg routine presented in this article used only data collected at the WWPS Pretorialaan (89 manually labelled images), and thus direct transferability of the classification algorithm to other stations cannot be guaranteed. Further work should aim at generalizing the FOG layer detection (transfer-learning) to a wider variety of pump

sumps.

The monitoring solution presented is also capable of in-situ processing of images. We used an embedded camera system with a Linux based micro-computer (Raspberry pi 4 Model B) which could run the Semantic-Segmentation machine-learning routine for the detection of FOG layers in 9.8 seconds per image at the camera itself. Hence, the system can be deployed in the field and the data transfer can be limited

to the post-processed variables alone, thus avoiding heavy raw-image data transfer. In-sensor deep-learning processing, also known as Edge AI computing (Deng et al., 2020) aims at leveraging inexpensive hardware for low-power inference of ML algorithms (e.g. NVIDIA Jetson Nano or google coral TPUs) to reduce data transfer requirements by in-situ processing. This would allow for on-site observation of variables in remote locations with low-power low-bandwidth data links (e.g. LoRaWAN satellite links, Fraire et al., 2020). We believe that the presented application here shows a promising potential for monitoring other emerging bio-hazards in hydro-ecological environments, for instance monitoring of algae-blooms, plastic litter, fauna, sediment plumes or other processes in remote locations.

In long-term monitoring of FOG, the adoption of a reproducible and robust optical calibration (corresponding frame-to-world coordinates) routine is encouraged. This should aim at restoring and allowing for continuity of the measurement series even under major disturbance of the camera position (e.g. cameras moved/disrupted during external maintenance). Also, due to the complex geometries found in WWPS sumps, the installation of multiple cameras is often required. This results in the need for robust image-stitching (mosaicking) routines.

Top-view pump sump imagery can also be used to derive additional relevant variables for the operation of the pumping station. The use of calibrated optical-gauges for the estimation of water level data could help retrieving data in un-gauged locations, assist in model calibration (de Vitry and Leitão, 2020) or act as a redundant sensor to detect failures of WWPS water level sensors (e.g. clogging, de-synchronization). Additionally, particle tracking velocimetry can be exploited to estimate the flow surface velocimetry, the flow circulation and vorticity at the pump sump. These variables are of high-interest for the management of WWPS since they could be used to detect the presence of air-entrapping free-surface vortices and as tools for assisting real-time control systems. Nevertheless, there are aspects of the surface velocity estimation that remains to be further investigated, for instance assessing the slip between flow and particle or the definition of robust parameters for (PTV/PIV) imagery in pump sumps (e.g. time delta, pixel resolution etc.). On the other hand, the FOG layer monitoring system constitutes a ready to use data source for the planning of FOG removal and maintenance operations.

One of the major limitations of the current measurement solution is that the top-view camera can only retrieve FOG surface characteristics, and thus neglects vertical growth and associated dynamics. Due to the buoyant and disaggregated nature of the loose FOG solids, this does not seem to affect the ability to capture long-term accumulation of FOG solids until the full surface of the sump is covered by a FOG layer. Further research is needed to devise a robust sensor for continuous monitoring of the layer depth and thus complement the measurements described in the present study.

To the authors' knowledge this is the first documented long-term high-frequency FOG layer dynamics database for WWPS. We believe that acquiring examples in a larger number of pumping stations would allow to describe fundamental processes involving accumulation and transport of FOG solids. Further research should aim at exploring FOG growth under the inherent variability of drainage systems (i.e. catchment/climatic characteristics, pipe network geometry, social habits etc.).

Declaration of Competing Interest

The authors declare that they have no known competing financial interests or personal relationships that could have appeared to influence the work reported in this paper.

Acknowledgements

Supplementary materials

Supplementary material associated with this article can be found, in the online version, at doi:10.1016/j.watres.2021.117482.

Appendix A. WWPS FOG layer Examples

Fig. A1, Fig. A2, Fig. A3.

Appendix B. Hardware and installation

Fig. B1, Fig. B2.

Appendix C. Restrictions due to the COVID-19 pandemic

Fig. C1.

Appendix D. Dataset video animation

Link to electronic supplementary material video: https://www.youtube.com/watch?v=R_G7hVlTje8

Appendix E. Particle tracking velocimetry

Fig. E1.

References

Abadi, M., Barham, P., Chen, J., Chen, Z., Davis, A., Dean, J., Devin, M., Ghemawat, S., Irving, G., Isard, M., Kudlur, M., 2016. Tensorflow: A system for large-scale machine learning. In: 12th USENIX symposium on operating systems design and implementation (OSDI 16), pp. 265–283.

Adams, T. (2018). London's fatberg on show: 'We thought of pickling it'. The Guardian, 4. https://www.theguardian.com/culture/2018/feb/04/fatberg-museum-london-display-pickling-age-waste.

Adrian, R.J., Westerweel, J., 2011. Particle image velocimetry (No. 30). Cambridge University Press.

Agüí, J.C., Jimenez, J., 1987. On the performance of particle tracking. J. Fluid Mech. 185, 447–468.

American National Hydraulic Standards Institute (2012). American National Standard for rotodynamic pumps for pump intake design. ANSI 9.8-2012. ISBN 978-880952-70-2.

Ashley, R.M., Fraser, A, Burrows, R., Blanksby, J., 2000. The management of sediment in combined sewers. Urban Water 2 (4), 263–275. https://doi.org/10.1016/S1462-0758(01)00010-3, 2000.

Blumensaat, F., Leitão, J.P., Ort, C., Rieckermann, J., Scheidegger, A., Vanrolleghem, P. A., Villez, K., 2019. How urban storm-and wastewater management prepares for emerging opportunities and threats: digital transformation, ubiquitous sensing, new data sources, and beyond-a horizon scan. Environ. Sci. Technol. 53 (15), 8488–8498.

Bradski, G., 2000. The OpenCV Library. Dr. Dobb's J. Softw. Tools.

de Vitry, M.M., Leitão, J.P., 2020. The potential of proxy water level measurements for calibrating urban pluvial flood models. Water Res. 175, 115669.

den Bieman, J.P., van Gent, M.R., van den Boogaard, H.F., 2020. Wave overtopping predictions using an advanced machine learning technique. Coastal Eng., 103830 https://doi.org/10.1016/j.coastaleng.2020.103830.

Deng, J., Dong, W., Socher, R., Li, L.J., Li, K., Fei-Fei, L., 2009. Imagenet: A large-scale hierarchical image database. In: 2009 IEEE conference on computer vision and pattern recognition. IEEE, pp. 248–255.

Deng, S., Zhao, H., Fang, W., Yin, J., Dustdar, S., Zomaya, A.Y., 2020. Edge intelligence: the confluence of edge computing and artificial intelligence. IEEE Internet of Things J. 7 (8), 7457–7469.

Duinmeijer, S.P., Moreno-Rodenas, A.M., Lepot, M., van Nieuwenhuizen, C., Meyer, I., Clemens, F.H., 2019. A simple measuring set-up for the experimental determination of the dynamics of a large particle in the 3D velocity field around a free surface vortex. Flow Meas. Instrum. 65, 52–64.

Duinmeijer, S.P.A., 2020. On the free-surface vortex driven motion of buoyant particles. Doctoral Thesis. Delft University of Technology. https://doi.org/10.4233/uuid:a33fa2a9-f347-40a3-96be-51e880018974.

Duinmeijer, S.P.A., Clemens, F.H.L.R., 2016. Experimental research on free-surface vortices as transport mechanism in wastewater sumps. In: 8th International Conference on Sewer Processes and Networks. Rotterdam, The Netherlands.

Fraire, J.A., Henn, S., Dovis, F., Garello, R., Taricco, G., 2020, December. Sparse Satellite Constellation Design for LoRa-based Direct-to-Satellite Internet of Things. In: GLOBECOM 2020-2020 IEEE Global Communications Conference. IEEE, pp. 1–6.

Garcia-Garcia, A., Orts-Escolano, S., Oprea, S., Villena-Martinez, V., & Garcia-Rodriguez, J. (2017). A review on deep learning techniques applied to semantic segmentation. arXiv preprint arXiv:1704.06857.

He, X., Francis Iii, L., Leming, M.L., Dean, L.O., Lappi, S.E., Ducoste, J.J., 2013. Mechanisms of fat, oil and grease (FOG) deposit formation in sewer lines. Water Res. 47 (13), 4451–4459.

Jeanbourquin, D., Sage, D., Nguyen, L., Schaeli, B., Kayal, S., Barry, D.A., Rossi, L., 2011. Flow measurements in sewers based on image analysis: automatic flow velocity algorithm. Water Sci. Technol. 64 (5), 1108–1114.

Jiang, J., Liu, J., Cheng, C., Huang, J., Xue, A., 2019. Automatic estimation of urban waterlogging depths from video images based on ubiquitous reference objects. Remote Sens. 11, 587. https://doi.org/10.3390/rs11050587.

Jolis, D., Loiacono, J., Kwan, L/, Sierra, N, Ving, K., Martis, M., 2010. Co-location of brown grease to biodiesel production facility at the oceanside wastewater treatment plant in San Francisco, CA. In: Proc. WEFTEC 2010, New Orleans Morial Conv. Centrer, Lousiana, USA, Water Environment Federation, pp. 6816–6829.

Keener, K.M., Ducoste, J.J., Holt, L.M., 2008. Properties influencing fat, oil, and grease deposit formation. Water Environ. Res. 80 (12), 2241–2246.

Korving, H., Clemens, F.H., van Noortwijk, J.M., 2006. Statistical modeling of the serviceability of sewage pumps. J. Hydraul. Eng. 132 (10), 1076–1085.

Martins, R., Rubinato, M., Kesserwani, G., Leandro, J., Djordjević, S., Shucksmith, J.D., 2018. On the characteristics of velocities fields in the vicinity of manhole inlet grates during flood events. Water Resour. Res. 54 (9), 6408–6422.

Miot, A., Jones, B.M., Ving, K., Noibi, M., Lukicheva, I., Jolis, D., 2013. Restaurant trap waste characterization and full scale FOG co-digestion at the San Francisco Oceanside Plant. In: Proc. WEFTEC 2013. McCormick Place, Chicago. Water Environment Federation, pp. 817–834.

Moy de Vitry, M., Kramer, S., Wegner, J.D., Leitão, J.P., 2019. Scalable flood level trend monitoring with surveillance cameras using a deep convolutional neural network. Hydrol. Earth Syst. Sci. 23 (11), 4621–4634. https://doi.org/10.5194/hess-23-4621-2019.

Naves, J., Anta, J., Suárez, J., Puertas, J., 2020. Hydraulic, wash-off and sediment transport experiments in a full-scale urban drainage physical model. Sci. Data 7 (1), 1–13.

Naves, J., García, J.T., Puertas, J., Anta, J., 2021. Assessing different imaging velocimetry techniques to measure shallow runoff velocities during rain events using an urban drainage physical model. Hydrol. Earth Syst. Sci. 25 (2), 885–900.

Nieuwenhuis, E., Post, J., Duinmeijer, A., Langeveld, J., Clemens, F., 2018. Statistical modelling of Fat, Oil and Grease (FOG) deposits in wastewater pump sumps. Water Res. 135, 155–167.

Leitão, J.P., Peña-Haro, S., Lüthi, B., Scheidegger, A., de Vitry, M.M., 2018. Urban overland runoff velocity measurement with consumer-grade surveillance cameras and surface structure image velocimetry. J. Hydrol. 565, 791–804.

OpenCV manual (2014). The OpenCV Reference Manual edition 3.4.14 https://docs.opencv.org/3.4/db/d58/group__calib3d__fisheye.html.

Pastore, C., Barca, E., Del Moro, G., Lopez, A, Mininni, G., Mascolo, G., 2015. Recoverable and reusable aluminium solvated species used as a homogeneous catalyst for biodiesel production from brown grease. Appl. Catal. A Gen. 501, 48–55. https://doi.org/10.1016/j.apcata.2015.04.031.

Pagnutti, M.A., Ryan, R.E., Gold, M.J., Harlan, R., Leggett, E., Pagnutti, J.F., 2017. Laying the foundation to use Raspberry Pi 3 V2 camera module imagery for scientific and engineering purposes. J. Electron. Imaging 26 (1), 013014.

Pothof, I.W.M., 2011. Co-current air-water flow in downward sloping pipes: Transport of capacity reducing gas pockets in wastewater mains. Doctoral Thesis. Delft University of Technology.

Regueiro-Picallo, M., Suárez, J., Sañudo, E., Puertas, J., Anta, J., 2020. New insights to study the accumulation and erosion processes of fine-grained organic sediments in combined sewer systems from a laboratory scale model. Sci. Total Environ. 716, 136923.

Shahsavari, G., Arnaud-Fassetta, G., Campisano, A., 2017. A field experiment to evaluate the cleaning performance of sewer flushing on non-uniform sediment deposits. Water Res. 118, 59–69.

Simonyan, K. & Zisserman, A. (2014). Very deep convolutional networks for large-scale image recognition. Arxiv preprint Arxiv:1409.1556.

Veldhuis, Ten, E., J.A., Clemens, F.H.L.R., Sterk, G., Berends, B.R, 2010. Microbial risks associated with exposure to pathogens in contaminated urban flood water. Water Res. 44 (9), 2910–2918.

Valero, D., Schalko, I., Fiedrich, H., Abad, J.D., Bung, D.B., Donchyts, G., Felder, E., Ferreira, R.M.L., Hohermuth, B., Kramer, M., Li, D., Mendes, L., Moreno-Rodenas, A., Nones, M., Paron, P., Ruiz-Villanueva, V., Wang R.-Q., Franca, M.J., (2021) Pathways towards democratization of hydro-environment observations and data. IAHR White paper series Issue 1. https://static.iahr.org/library/AnythingElse/WhitePaper/2021_1_Democratization_Hydro_Environment_Observations_Data.pdf.

Wallace, T, Gibbons, D., O'Dwyer, M., Curran, T, 2016. International evolution of fat, oil and grease (FOG) waste management- A review. J. Environ. Manage. https://doi.org/10.1016/j.jenvman.2016.11.003.

Williams, J.B., Clarkson, C., Mant, C., Drinkwater, A., May, E., 2012. Fat, oil and grease deposits in sewers: Characterisation of deposits and formation mechanisms. Water Res. 46 (19), 6319–6328.

Ye, J.C., Sung, W.K., 2019. Understanding geometry of encoder-decoder CNNs. In: International Conference on Machine Learning. PMLR, pp. 7064–7073.